Check for updates

Two different pore architectures of cyamelurate-based metal–organic frameworks for highly selective CO₂ capture under ambient conditions†

Mohamed Essalhi, [ID] *[a] Midhun Mohan, [ID] [a] Nour Dissem, [ID] [a] Najmedinne Ferhi, [ID] [a] Adela Abidi, [ID] [a] Thierry Maris [ID] [b] and Adam Duong [ID] *[a]

In the context of porous coordination materials toward CO_2 capture and separation, two new metal–organic frameworks termed IRH-**6** and IRH-**7** were synthesized with square and rhombic microchannel pores, respectively. These materials exhibit high CO_2 uptakes of 2.67 mol kg^{-1} (IRH-**6**) and 2.78 mol kg^{-1} (IRH-**7**) at 100 kPa and 298 K. Grand canonical Monte Carlo simulation demonstrated strong non-covalent interactions between quadripolar CO_2 molecules and these nitrogen-rich frameworks. CO_2/CH_4 (50 : 50), CO_2/N_2 (15 : 85), and CO_2/H_2 (15 : 85) gas mixtures were investigated by ideal adsorbed solution theory and showed excellent CO_2 selectivity under ambient conditions for both porous materials. In particular, a remarkable increase in the CO_2 selectivity to 102 for IRH-**7** over 31 for IRH-**6** was observed for the CO_2/CH_4 binary mixture, which highlights the effect of pore aperture modification on preferential CO_2 uptake over other conventional gases.

Introduction

Anthropogenic carbon dioxide (CO_2) emissions have attracted much concern over recent decades in order to find practical solutions to critical climate change issues.[1] Worldwide programs and policies have been implemented to tackle climate challenges, which significantly reduce anthropogenic CO_2 emissions. In parallel, scientists have developed promising technologies for CO_2 capture and sequestration, and have developed alternative energy systems that work with renewable energy to reduce CO_2 emissions.[2–4] Impressive efforts have been invested in developing efficient CO_2 capture materials such as inorganic[5–7] and organometallic porous materials.[8–11]

As an emerging subclass of porous coordination polymers, metal–organic frameworks (MOFs) have been widely studied for their remarkable features such as high specific surface areas, tunable porosity, thermal and chemical stability, and so

[a]Département de Chimie, Biochimie et physique, Institut de Recherche sur l'Hydrogène, Université du Québec à Trois-Rivières, Trois-Rivières, Québec, G9A 5H7, Canada. E-mail: mohamed.essalhi@uqtr.ca, adam.duong@uqtr.ca
[b]Département de Chimie, Université de Montréal, Montréal, Québec, H3C 3J7, Canada

†Electronic supplementary information (ESI) available: Additional crystallographic details (including thermal atomic displacement ellipsoid plots), mass spectrum, ORTEP diagrams, and other crystallographic data, powder X-ray diffraction, infrared, thermogravimetry analysis, and photographs of the crystalline samples (PDF). CCDC 2104590–2104592. For ESI and crystallographic data in CIF or other electronic format see DOI: https://doi.org/10.1039/d2qi02208g

forth.[12] The functionalization of these materials allows better interactions with guest molecules and improves their retention as well as their catalytic conversion, which makes MOFs promising materials for diverse applications.[13] Over the last few decades, MOFs have been reported as successful platforms for several valuable applications such as gas capture and sequestration, catalysis and chemical conversion, electrochemical applications, chemical detection, water treatment, drug delivery, and white light emission.[14–21] In particular, a special category of microporous MOFs was proved to be efficient for selective CO_2 capture, featuring both a tailor-made framework and perfect surface potential constructed exclusively to host CO_2 molecules.[22–24] The design of such materials can be achieved under solvothermal synthesis conditions using polytopic organic linkers and metal ions. The structure of organic linkers and the coordination mode of metal ions facilitate the architecture prediction of MOFs.[25] To date, many strategies have been adopted to design MOFs with high CO_2 retention, such as incorporating active Lewis sites and polar functional groups in ligands and creating open metal sites within the frameworks, which enhanced MOFs performances for gas mixtures separation, mainly for CO_2 over N_2, H_2, C_2H_2, and CH_4.[26–31] However, the geometric prediction of MOFs remains random, leaving sometimes a large gap between the desired structure and the obtained one, which can affect the MOF properties. In this case, post-synthetic modification of MOFs is required to get the desired performances. This study reports the successful synthesis and characterization of two new microporous neody-

This journal is © the Partner Organisations 2023

Inorg. Chem. Front., 2023, **10**, 1037–1048 | **1037**

mium-based MOFs termed IRHs **6** and **7** (IRH = *Institut de Recherche sur l'Hydrogène*) with two different pore apertures supported by nitrogen-rich cyamelurate (**Cy**) linkers.[32] Furthermore, a successful structural modification from the square pore aperture in IRH-**6** to the rhombic one in IRH-**7** *via* the **Cy**–Nd intermediate complex has improved the selective CO_2 uptake over CH_4. The strategic design of these microporous MOFs is based on the small size of **Cy** linkers and the high coordination number of oxyphilic Nd^{3+} ions. In addition, abundant heteroatoms (O and N) incorporated in **Cy** linkers ensure a good amount of accessible Lewis-base sites which enhance selective CO_2 capture over other gases (CH_4, N_2, H_2).

Results and discussion

In our previous work, we have provided an instance of selective CO_2 adsorption for three lanthanide-based MOFs supported by the **Cy** linker termed IRHs-**1**–**3** where the preferential CO_2 uptake has been improved by the small pore size and the nitrogen-rich surface.[33] Herein, our study aims to evaluate the effect of aperture modification of novel neodymium-based MOFs to improve their preferential CO_2 adsorption. Under solvothermal conditions, we synthesized a new MOF isomorphous to the IRH (**1**–**3**) series denoted as IRH-**6** with a square pore aperture. Furthermore, this framework was broken down under hydrothermal conditions to an intermediate molecular complex denoted **Cy**–Nd with seven coordinated water molecules, which was subsequently used to reconstruct again a new tridimensional framework

termed IRH-**7**. This new MOF was obtained by the self-assembly of **Cy**–Nd molecules under solvothermal conditions. In a water-deficient medium, the Nd^{3+} metal ions of the **Cy**–Nd complex change their coordination environment by releasing five coordinated water molecules, and binding to the free O–N coordination sites of the Cy^{-1} anion by auto-assembly. This mechanism leads to the reconstruction of a new extended IRH-**7** with a rhombic pore aperture (Fig. 1). In our previous work, we have highlighted different possible coordination modes of cyamelurate–lanthanide systems, resulting in four different types of coordination systems; we observed the Ln contraction effect on the ionic radii, which affects the coordination spheres along the lanthanide series.[34] Herein, because of the position of its ionic radius in the series, the Nd^{3+} ion allows different coordination modes and jumps from a simple molecular complex configuration to an extended 3D coordination network.

Structural description

The structural elucidation by single-crystal X-ray diffraction (SCXRD) shows a porous structure for IRH-**6** with the general formula $[Nd(Cy)(H_2O)_2]_n$ crystallizing in the $P4_122$ space group of the tetragonal system. A symmetrical view of IRH-**6** structure (Fig. S1†) shows that **Cy** linkers bonded to four Nd^{3+} ions by coordination bonds to both oxygen and nitrogen sites, and thus Nd^{3+} ions exhibit a coordination number of 10 provided by four **Cy** and two H_2O molecules. Each **Cy** linker displays the μ_4-bridging coordination mode into 4-connected nodes while each metal ion acts as a 4-c node to form a rigid three-dimen-
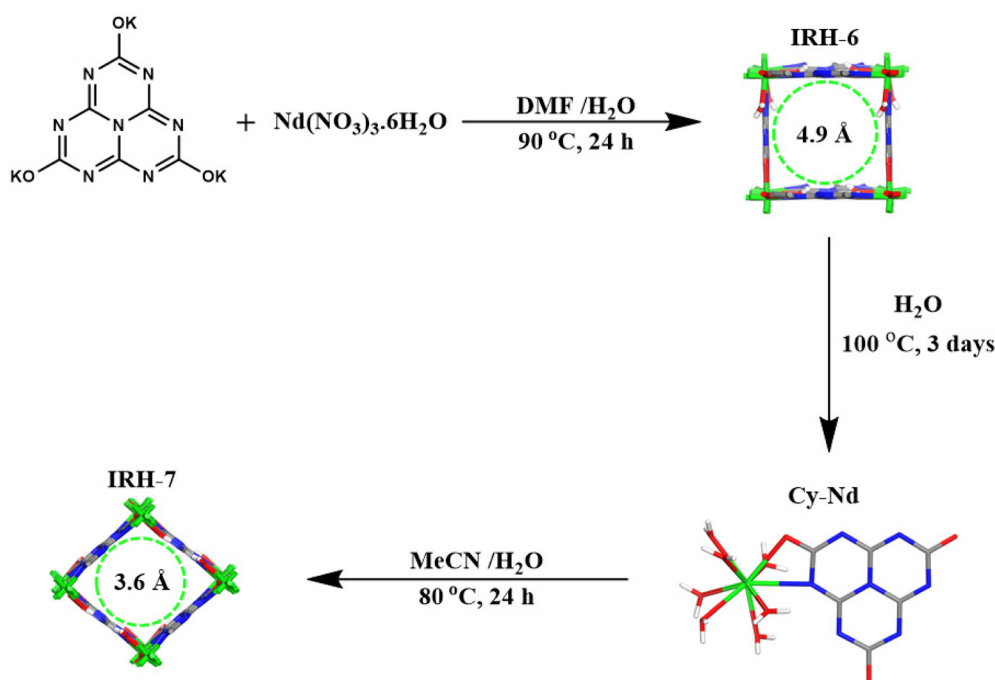

Fig. 1 Synthesis routes of IRH-**6**, **Cy**–Nd and IRH-**7**.

sional microporous framework of the square pore aperture and the pts-sqc183 topology (Fig. 2a–c).

In water medium at 100 °C for 3 days, IRH-**6** breaks down to the heptahydrate molecular complex of **Cy**–Nd with the general formula $[Nd(Cy)(H_2O)_7]_n$ which crystallizes in the $P2_1/n$ space group of the monoclinic system. In this structure, Nd^{3+} ions have an ennea-coordination environment of $NdNO_8$ (Fig. S2 and S3†) formed by seven oxygen atoms from seven water molecules, and one nitrogen and one oxygen atom from a **Cy** linker in a slightly distorted tricapped trigonal prism around the Nd^{3+} ion. In an acetonitrile/water (10 : 1) mixture at 80 °C, metal knots of **Cy**–Nd lose five coordinated water molecules and recombine to form the tridimensional framework of IRH-**7** with a rhombic pore aperture (Fig. 2d), in which the **Cy** linkers have the same coordination mode as that in IRH-**6** (Fig. S4†). However, different bond angles and space groups are obtained (Table S1†). IRH-**7** has a general formula of $[Nd(Cy)(H_2O)_2]_n$ and crystallizes in the $C222_1$ space group of the orthorhombic system with the simplified topology of pts-sqc183 (Fig. 2e and f). IRHs **6** and **7** exhibit effective accessible pore apertures of about 4.9 Å and 3.6 Å (regardless of the van der Waals radii), respectively. As illustrated in Fig. S5 and S6†, the guest accessible void volume was assessed to be 43% (IRH-**6**) and 42% (IRH-**7**) of the unit cell volume as determined using PLATON.[35] All crystallographic data are given in Table S1† and the selected coordination bonds and angles are given in Tables S2–S10.†

Characterizations

The phase purity of the as-synthesized IRH-**6**, **Cy**–Nd, and IRH-**7** was investigated by comparing simulated and experimental powder X-Ray diffraction (PXRD) patterns (Fig. S7–S9†). This result was strengthened by the scanning electron microscopy (SEM) images, which substantiate the identical crystal morphologies of the as-synthesized samples with an average size of 50–200 μm without contamination by amorphous phases. The SEM (Fig. 3) and optical images (Fig. S10–S12†) show octahedral crystals for IRH-**6** and elongated needles for IRH-**7**, while **Cy**–Nd exhibits parallelepiped crystals.

IRHs **6** and **7** were activated before gas sorption measurements. A solvent exchange process for 48 hours was carried out in anhydrous methanol which was regenerated every 8 hours. Thereafter, a final activation was carried out overnight at 110 °C in a dynamic vacuum to provide activated IRHs **6** and **7**. FTIR and PXRD analyses were performed to investigate the crystallinity and chemical stability of IRHs **6** and **7** during the activation process. The PXRD patterns of the solvent exchanged and activated samples of IRHs **6** and **7** were in good agreement with those of the simulated patterns (Fig. S7 and S8†). Furthermore, the FTIR spectra of the as-synthesized IRHs **6** and **7** were unveiled and were similar to those after solvent exchange and also after the complete activation (Fig. S13 and S14†). Besides, their thermal stability was tested using a TG analyzer under a nitrogen atmosphere in a temperature range
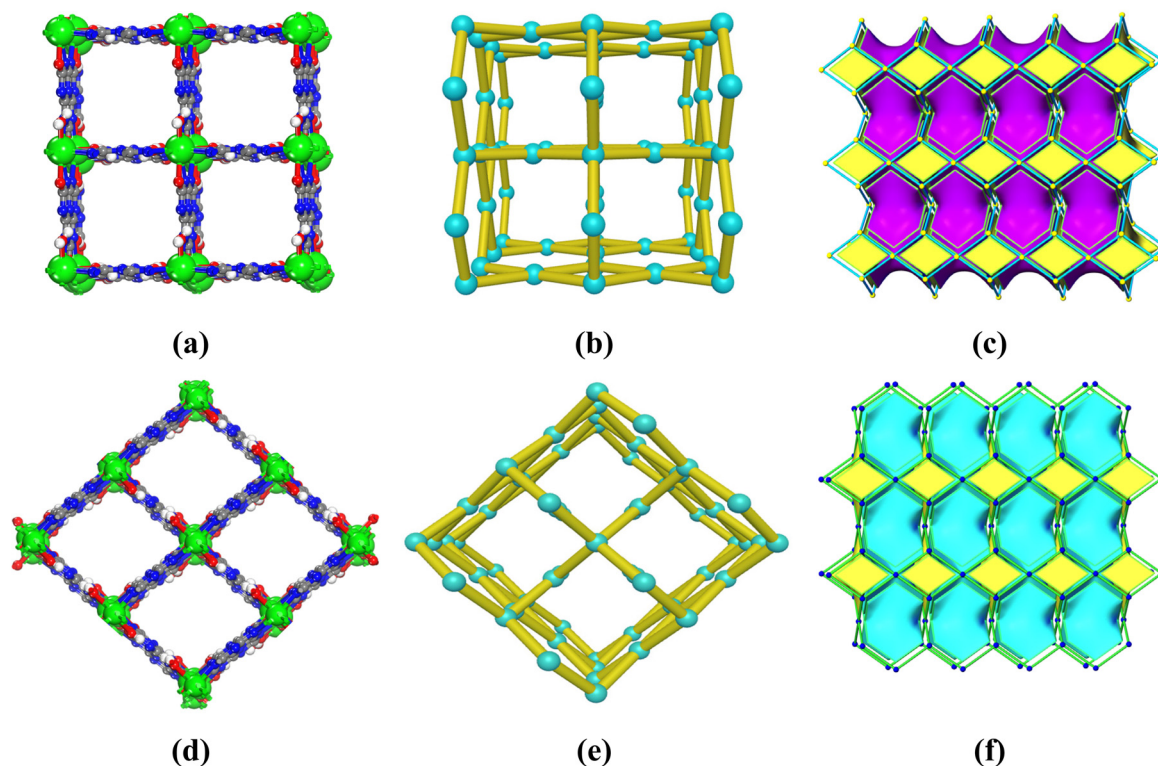

Fig. 2 Views of pores structures, corresponding topology, and respective tilling for (a–c) IRH-**6** and (d–f) IRH-**7**. Carbon atoms are shown in gray, oxygen atoms in red, hydrogen atoms in white, nitrogen atoms in blue, and neodymium atoms in green.
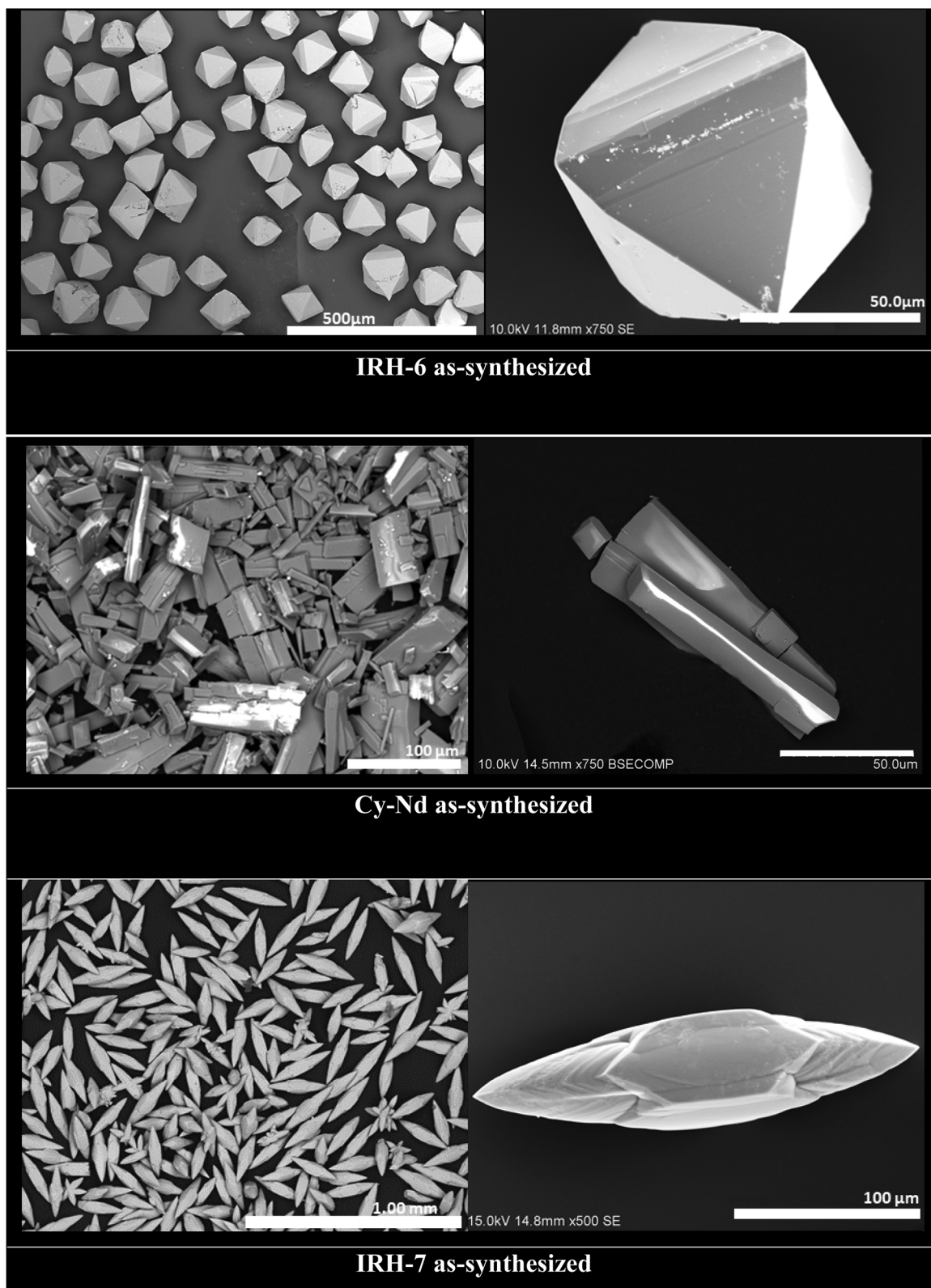
Fig. 3 SEM images of the as-synthesized phases of IRH-**6**, **Cy**–Nd, and IRH-**7**.

of 30–800 °C (10 °C min^{-1}). The results are displayed in Fig. S16 and S17.† The TG curves of the as-synthesized IRHs 6 and 7 show a first weight loss of 5% and 7% respect-

ively, starting at ~110 and 115 °C, which can be assigned to the release of free H_2O molecules in the pores. The solvent exchange curves disclose a first weight loss of 5% (IRH-**6**) and

1040 | *Inorg. Chem. Front.*, 2023, **10**, 1037–1048

This journal is © the Partner Organisations 2023

7.5% (IRH-**7**) starting at ~35 °C, which is assigned to the release of the exchanged MeOH molecules. Common weight loss at ~180 °C was observed for the as-synthesized, exchanged, and activated IRHs **6** and **7**, which can be attributed to the release of coordinated H_2O molecules in the frameworks.[33] After that, no weight loss was observed up to ~400 °C. TGA and FTIR analysis confirmed the total activation of IRHs **6** and **7**, indicating the complete removal of solvent guest molecules from the frameworks. The good chemical and thermal stability in addition to the permanent porosity of IRHs **6** and **7**, provides a good basis for the subsequent adsorption tests.

Gas adsorption studies

CO_2 adsorption isotherms collected at 273 K show a type-I adsorption isotherm (Fig. S19†) for the activated IRHs **6** and **7**, thus highlighting their permanent porosity. The experimental Brunauer–Emmett–Teller surface areas for IRH-**6** and IRH-**7** were about 501 m^2 g^{-1} and 462 m^2 g^{-1}, respectively; these values were slightly lower than the theoretical ones calculated for IRH-**6** (652 m^2 g^{-1}) and IRH-**7** (547 m^2 g^{-1}). Furthermore, IRHs **6** and **7** depict uniform microporous structures with an experimental mean pore size of 5.4 Å for IRH-**6** and 3.6 Å for IRH-**7**, which are consistent with the theoretically calculated values of 4.9 Å and 3.6 Å for IRH-**6** and IRH-**7**, respectively (Table S11†).

Gas diffusion within the framework is directly related to the kinetic diameter of the gaseous molecules (Table S12†);[36] thus the design of tailored pores regarding the mean path of guest gas molecules and their collisions with the pore aperture remains the most promising gas separation technique. IRH **6** and **7** pore sizes and shapes, their permanent porosity, and nitrogen-rich surfaces support their preferential CO_2 capture. The experimental adsorption isotherms are illustrated in Fig. 4 and adsorption capacities are given in Table S13.† The CO_2 adsorption isotherms of IRHs **6** and **7** exhibit exponential adsorption isotherms saturated under high pressures. CO_2 uptakes quickly reach high adsorption values of 2.67 mol kg^{-1} for IRH-**6** and 2.78 mol kg^{-1} for IRH-**7** under 100 kPa at 298 K. This behavior can be attributed to favorable electrostatic interactions of CO_2 with the nitrogen sites and the coordinated water molecules incorporated in the frameworks, and to the kinetic diameter of CO_2 molecules suitable with the pore aperture of these frameworks. N_2 and H_2 adsorptions were much lower and those under 100 kPa at 298 K were only 0.07 mol kg^{-1} (N_2) and 0.05 mol kg^{-1} (H_2) for IRH-**6** compared to those of IRH-**7**, which do not exceed 0.05 mol kg^{-1} (N_2) and 0.06 mol kg^{-1} (H_2) under the same conditions. These low adsorption values can be explained by the weak electrostatic interactions of H_2 and N_2 nonpolar gases with these nitrogen-rich frameworks. A remarkable decrease in CH_4 uptake was observed for IRH-**7** (0.08 mol kg^{-1}) over IRH-**6** (1.03 mol kg^{-1}) under 100 kPa at 298 K. This can be justified by the narrowing of the pore aperture of IRH-**7**, which significantly reduces the adsorption of CH_4 of kinetic diameter greater than the pore diameter of this porous material.[37] IRHs **6** and **7** maintain the same
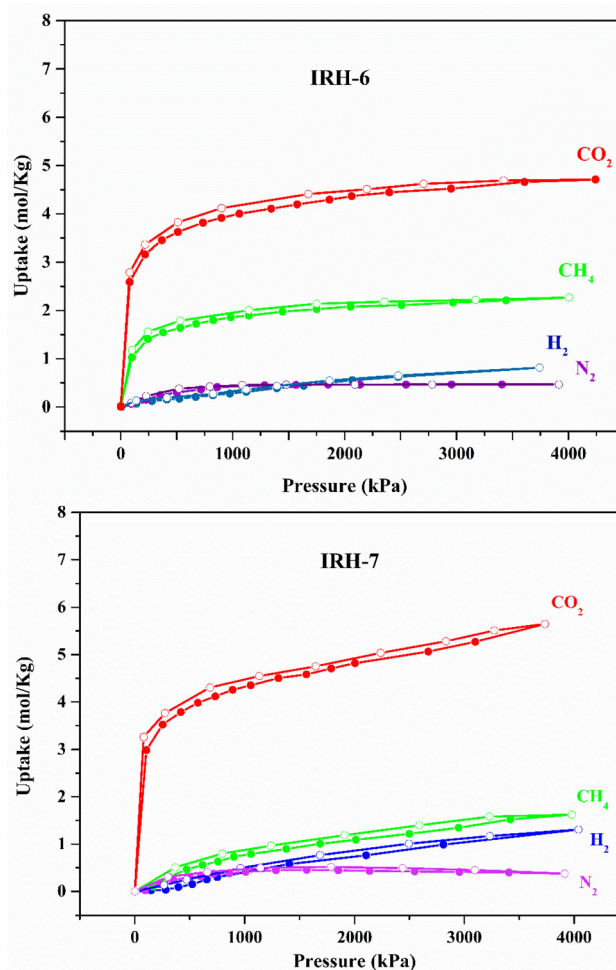

Fig. 4 Experimental adsorption isotherms of CO_2, CH_4, N_2, and H_2 at 298 K for IRH-**6** and IRH-**7**.

exponential CO_2 adsorption behavior after several adsorption cycles without any loss of capacity (Fig. S20 and S21†). The PXRD patterns after adsorption, heated to 130 °C and 160 °C and exposed to humidity, match well those of the as-synthesized ones, which confirms the stability of IRHs **6** and **7** under chemical and thermal stress conditions (Fig. S22 and S23†).

Molecular simulation

Grand Canonical Monte Carlo (GCMC) simulations were performed to further investigate the preferential CO_2 uptake of IRHs **6** and **7**. Basically, GCMC is a computational method based on random trial movement steps (insertion, translation, rotation) applied to sorbate molecules inside a simulation box containing a rigid frame. In this system, the chemical potential, temperature, and volume are maintained fixed, while sorbate–sorbate and sorbate–framework electrostatic and van der Waals interactions are continuously evaluated using universal force field (UFF) parameters and Lennard-Jones (LJ) potential; detailed descriptions are given in the Experimental

This journal is © the Partner Organisations 2023

Inorg. Chem. Front., 2023, **10**, 1037–1048 | **1041**

section.[38–40] We simulate the CO_2 density distributions under 100 kPa at 298 K within IRH **6** and **7** microchannel pores as shown in Fig. 5; the CO_2 molecules are distributed homogeneously in the pores and mainly occupy the center of the unidirectional channels. The intense blue regions over the probability density map indicate strong adsorption sites within the surfaces, which are located in between coordinated water molecules and in front of **Cy** nitrogen sites incorporated in both frameworks. The simulated annealing calculations disclose strong CO_2 binding sites near the coordinated H_2O molecules and the **Cy** nitrogen sites. No binding sites were observed around Nd^{3+} ions because their highly occupied coordination environment which blocks any contact with the CO_2 molecules. As illustrated in Fig. S24,† CO_2 molecules were electrostatically trapped in the framework through non-covalent interactions with the hydrogen atoms of coordinated H_2O molecules and nitrogen atoms of **Cy** linkers. A total of eight interactions with an average distance of 3.36 Å ($O5–H5A\cdots O1(CO_2)^1$, $O5–H5B\cdots O2(CO_2)^1$, $C3–N1\cdots O1(CO_2)^2$, $O4–H4A\cdots O2(CO_2)^2$, $O4–H4B\cdots O1(CO_2)^3$, $C3–N4\cdots O2(CO_2)^3$, $O4–H4B\cdots O1(CO_2)^4$, $C3–N4\cdots O2(CO_2)^4$) are responsible for holding CO_2 molecules in the framework and play the pivotal role for the high CO_2 selectivity.

Ideal adsorbed solution theory (IAST)

To further explore the CO_2 adsorption selectivity of IRHs **6** and **7**, ideal adsorbed solution theory (IAST) has been employed to predict the selectivity for CO_2/CH_4 (50 : 50), CO_2/N_2 (15 : 85), and CO_2/H_2 (15 : 85) gas mixtures, mimicking post/pre-combustion capture and natural gas sweetening situations.[41,42] The CO_2, CH_4, N_2, and H_2 single-component adsorption isotherms were fitted with the dual-site Langmuir–Freundlich
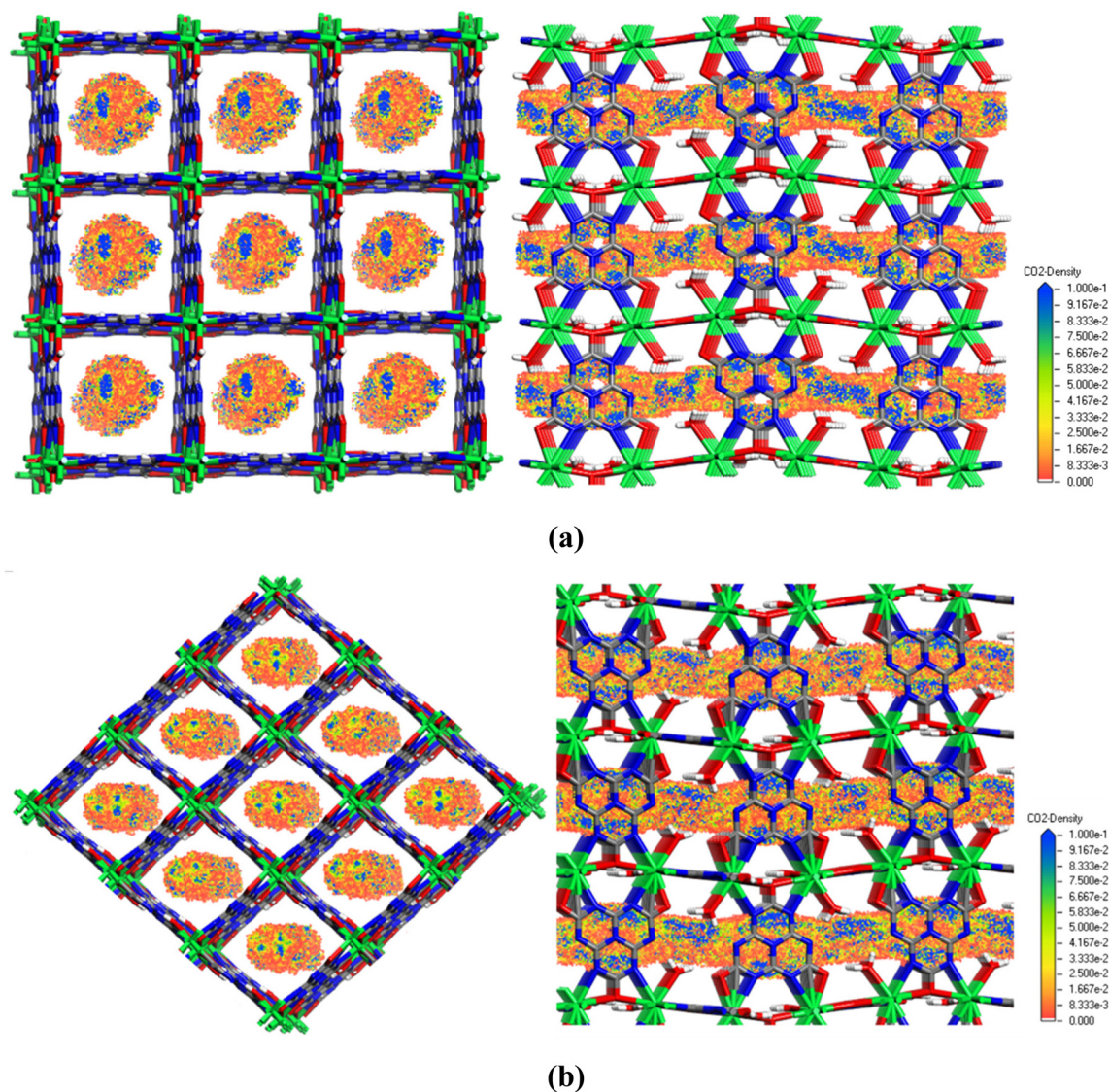

Fig. 5 (a) IRH-**6** and (b) IRH-**7** Monte-Carlo simulated CO_2 adsorption under 100 kPa at 298 K. Carbon atoms are shown in gray, oxygen atoms in red, hydrogen atoms in white, nitrogen atoms in blue, and neodymium atoms in green.

1042 | *Inorg. Chem. Front.*, 2023, **10**, 1037–1048

This journal is © the Partner Organisations 2023

(DSLF) model (eqn (S1)†).[43] Thereafter, the multi-component adsorption isotherms were predicted based on Gibbs adsorption equilibrium (eqn (S2)†) using the calculated fitting parameters (Table S14†). Simulated adsorption isotherms (Fig. 6) and IAST selectivities (S_{IAST}) were calculated following eqn (S3)† and further compared to those of selected materials from the literature (Table S15†). As expected, the CO_2 adsorption isotherms in all simulated mixtures for IRH-**6** and IRH-**7** have the same shape as that in the experimental isotherms with differences in absorption capacities. IRHs **6**–**7** exhibit a very fast adsorption tendency under low pressure to reach certain saturation under high pressure due to the favorable interactions of CO_2 within the frameworks. Moreover, N_2 and H_2 showed very low slope and adsorption capacity for both IRH structures, even at a low CO_2 concentration (15%) of simulated mixtures. As a result, IRH-**6** and IRH-**7** showed the same CO_2 selectivity factor of about 30 under 100 kPa at 298 K for the

CO_2/N_2 (15 : 85) mixture, which exceeded the selectivity factor of 26.6 reported for MOF-505-K[44] and reached the selectivity factor of 31 for COF F-DCBP-CTF-1 observed for the CO_2/N_2 (15 : 85) mixture under ambient conditions.[45] Similarly, IRH-**6** and IRH-**7** exhibit high selectivity factors of about 29 and 30, respectively, for the CO_2/H_2 (15 : 85) mixture under 100 kPa at 298 K, and are nearly equivalent to the industrial NaX and NaY zeolites with a high CO_2 selectivity factor of 29 under the same conditions.[46] Under high pressure, IRH-**6** and IRH-**7** show the corresponding selectivity factors of 35 and 39 for the CO_2/H_2 (15 : 85) mixture under 4000 kPa at 298 K, respectively. In addition, IRH-**7** shows a higher selectivity factor of 137 for the CO_2/N_2 (15 : 85) mixture compared to 55 exhibited by IRH-**6** under 4000 kPa at 298 K. These results demonstrate the promising potential of IRHs **6** and **7** for CO_2/N_2 and CO_2/H_2 separation due to their high affinity for the polar CO_2 molecules. On the other hand, the remarkable effect of the pore aperture
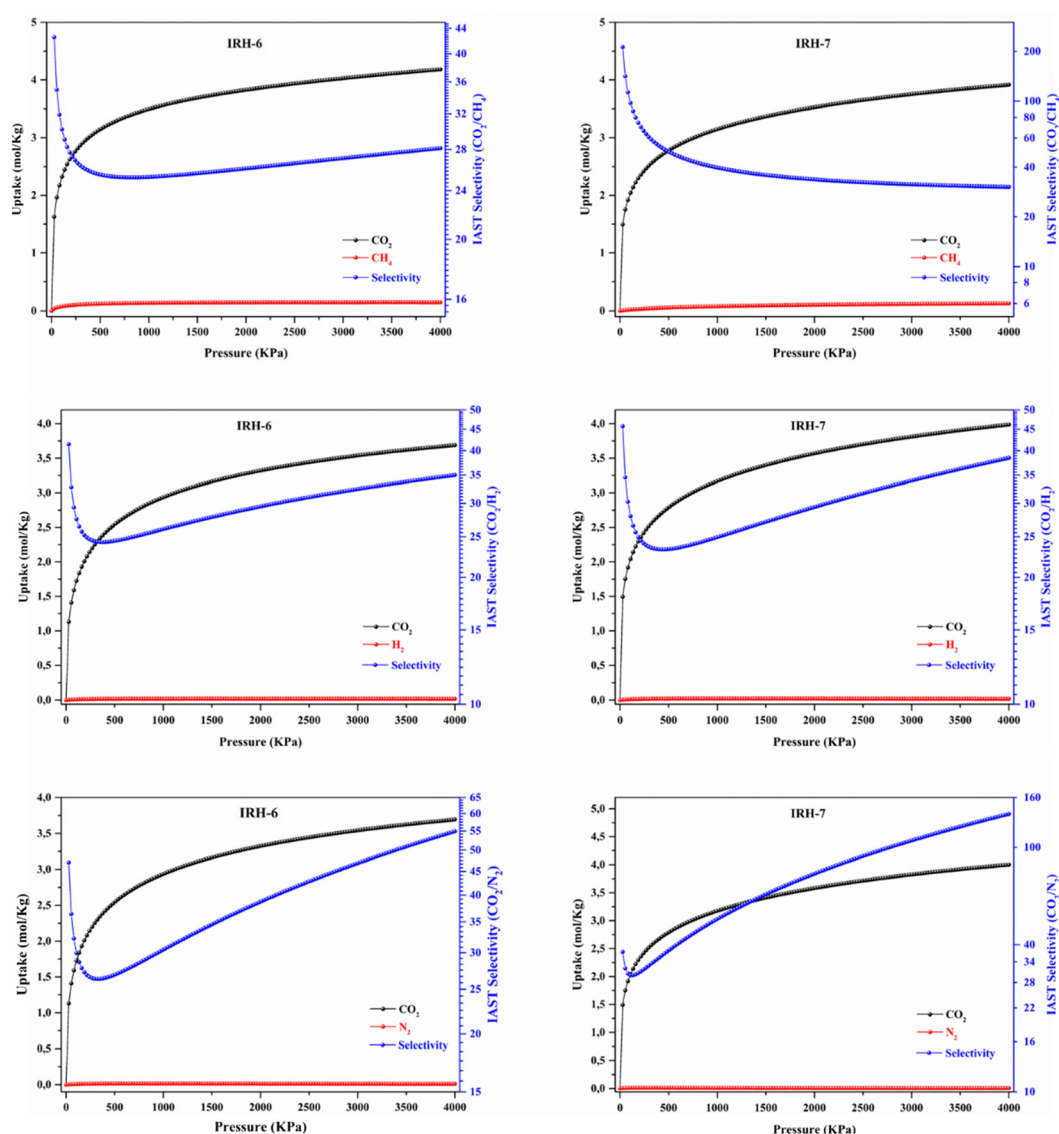

Fig. 6 IAST adsorption isotherms and CO_2 selectivity of IRHs **6** and **7** for the CO_2/CH_4 (50 : 50), CO_2/N_2 (15 : 85), and CO_2/H_2 (15 : 85) mixtures.

This journal is © the Partner Organisations 2023

Inorg. Chem. Front., 2023, **10**, 1037–1048 | **1043**

modification on increasing the CO_2 selectivity of IRH-**7** over IRH-**6** was demonstrated by the results of the CO_2/CH_4 (50:50) mixture. IRH-**6** shows a selectivity factor of 31 for the CO_2/CH_4 (50:50) mixture under 100 kPa at 298 K, which is comparable to the selectivity values of 27 for IRH-**3** under the same conditions.[33] This result is comparable to that of many previously reported MOFs, carbonaceous materials, and zeolites with good separation performance for the CO_2/CH_4 (50:50) mixture under ambient conditions such as UTSA-16 with a CO_2 selectivity factor of 29 [47] and nitrogen-doped porous carbon CPC-600 with a CO_2 selectivity factor of 26.[48] After successful modification of the pore aperture, IRH-**7** reached a selectivity factor of 102 for the CO_2/CH_4 (50:50) mixture under 100 kPa at 298 K which is comparable to exceptional UTSA-120 and zeolite-13X of high separation potential with selectivity factors of 96 and 103, respectively.[49,50] Since IRH-**6** and IRH-**7** have almost similar CO_2 adsorption isotherms, the difference in selectivity factors for the CO_2/CH_4 mixture (50:50) can be explained by the difference between the CH_4 adsorption capacity of IRH-**7** with a pore aperture smaller than the kinetic diameter of CH_4 and the adsorption capacity of IRH-**6** with a pore aperture higher than the kinetic diameter of CH_4 molecules. In the high-pressure range, the CH_4 adsorption capacity continued to increase moderately while the CO_2 adsorption capacity reached saturation for both materials in the simulated CO_2/CH_4 mixture, which explains the decrease in CO_2 selectivity of IRH-**6** and IRH-**7** to reach 31 and 102, respectively, under 4000 kPa at 298 K for the CO_2/CH_4 binary mixture.

Conclusion

In summary, we reported the successful synthesis and pore architecture modification of new microporous MOFs termed IRHs **6** and **7** supported by nitrogen-rich **Cy** linkers and Nd^{3+} ions. The structural study and porosity analysis unveil two distinct square and rhombic pore apertures for IRH-**6** and IRH-**7** with median pore sizes of about 4.9 and 3.6 Å, respectively. Gas sorption studies disclosed high CO_2 uptakes over CH_4, N_2 and H_2 for IRHs **6** and **7** under ambient conditions. Moreover, modification of the pore aperture for IRH-**7** significantly decreased its CH_4 uptake over IRH-**6**. The GCMC simulation showed strong binding sites for CO_2 molecules around the co-ordinated H_2O molecules and nitrogen sites incorporated into the IRH **6** and **7** microporous channels. In addition, IAST predicted excellent CO_2 selectivity of IRHs **6** and **7** for the CO_2/CH_4 (50:50), CO_2/N_2 (15:85), and CO_2/H_2 (15:85) mixtures under 100 kPa at 298 K. In particular, a remarkable selectivity factor of 102 of IRH-**7** for the CO_2/CH_4 (50:50) mixture and high CO_2 selectivities of about 30 for the CO_2/N_2, 29 and 30 for CO_2/H_2 (15:85) mixtures were observed for IRH **6** and **7**, respectively. These results demonstrated the efficiency of the designing microporous MOFs with polarized surfaces to selectively adsorb CO_2 molecules and highlighted the remarkable effect of pore aperture modification on increasing CO_2 selectivity.

Experimental

Materials and methods

All reagents and solvents employed were commercially available and used without further purification. The FTIR spectra were recorded with a Nicolet-iS-10 smart FTIR spectrometer using the transmittance mode within the 550–4000 cm^{-1} range to collect data. The thermogravimetry analysis was performed using Diamond Pyris TGA/DTA apparatus from PerkinElmer and Mettler Toledo TGA/DSC1 and all data were collected within 25–800 °C at a rate of 5 °C min^{-1}. The scanning electron microscopy images were recorded using an EFSEM JEOL model 5500. Crystallographic data were collected using a Bruker APEX2 diffractometer with Cu Kα radiation. The structures were solved by direct methods using SHELXT-2018,[51] and non-hydrogen atoms were refined anisotropically with least-squares minimization using SHELXL-2018.[52] Hydrogen atoms were treated by first locating them from difference Fourier maps, recalculating their positions using standard values for distances and angles, and then refining them as riding atoms. Powder X-ray diffraction data were collected on an Xcalibur & Gemini Rigaku diffractometer with a dual fine-focus X-ray source (Cu Kα radiation) at room temperature. The samples were gently ground and mounted on a nylon loop. The data collection involved acquisition in transmission geometry of four different sections with increasing angular position, giving four different 2D frames that were integrated and combined to produce the final 1D X-ray diffraction patterns. Simulated powder diffraction patterns were generated from the corresponding CIFs resulting from the single-crystal analysis using the Mercury software of the Cambridge Crystallographic Data Centre.[53] A unique value of the FWHM for the diffraction peaks was adjusted to obtain a better match between the resolution of the experimental and the calculated patterns.

Synthesis procedures

Potassium cyamelurate. Potassium cyamelurate ($K_3 \cdot$**Cy**) was synthesized according to the method described in the literature reported by E. Horvath-Bordon et al.[54]

IRH-6. Synthesis of IRH-**6** was carried out according to the solvothermal method using a mixture of equimolar solvents of DMF/H_2O. Typically, 33.5 mg (0.1 mmol) of potassium cyamelurate was solubilized in 8 mL of H_2O, and 353.1 mg (0.6 mmol) of neodymium salt ($Nd(NO_3)_3 \cdot 6H_2O$) was solubilized in 8 mL of N,N-dimethylformamide (DMF). The solutions were mixed at room temperature, stirred, and sonicated for 15 min. Thereafter, the mixture was sealed and heated at 90 °C for 24 hours. After cooling down to room temperature, as-synthesized IRH-**6** (purple octahedral crystals) was recovered by filtration and washed twice with methanol (90% yield).

Post-synthesis modification

Cy–Nd. The molecular complex of **Cy**–Nd was obtained by the destruction of the IRH-**6** framework under hydrothermal conditions. Typically, 100 mg of IRH-**6** previously washed a couple of times with water at room temperature and well

1044 | *Inorg. Chem. Front.*, 2023, **10**, 1037–1048

This journal is © the Partner Organisations 2023

crushed using a mortar was immersed in 12 mL of water, stirred, and sonicated for 30 min. Thereafter, the mixture was sealed and heated at 100 °C for 3 days. After cooling down to room temperature, the as-synthesized **Cy**–Nd molecular complex (purple parallelepiped crystals) was recovered by filtration, washed twice with acetone, and dried in a dynamic vacuum (70% yield).

IRH-7. Synthesis of IRH-7 consisted of reconstructing the 3D framework using the **Cy**–Nd complex as a precursor in a solution of neodymium ions in excess. Typically, 100 mg of **Cy**–Nd previously dried and well crushed using a mortar was immersed with 100 mg of neodymium salt ($Nd(NO_3)_3 \cdot 6H_2O$) in 16 mL of a mixture of $MeCN/H_2O$ (10 : 1), and the above mixture was stirred, and sonicated for 30 min. Thereafter, the mixture was sealed and heated at 80 °C for 24 hours. After cooling down to room temperature, as-synthesized IRH-7 (purple needle crystals) was recovered by filtration and washed twice with methanol (90% yield).

Gas adsorption measurement

Pure-gas adsorption isotherms were collected using a home-made pure gas volumetric device (VP) at 298 K.[55,56] Before the measurements, 200 mg of the activated sample was heated (degassed) in a vacuum at 298 K for 24 h. The single-gas adsorption isotherms were measured *via* the standard volumetric approach consisting of a known amount of gas initially stored in the reference volume before being expanded into the measurement cell volume. The balance between the initial and final conditions was used to calculate the adsorbed amount. The process was repeated continuously until the final equilibrium pressure was reached. Afterward, the reverse procedure was used to determine the desorption isotherm.

Ideal adsorbed solution theory (IAST) calculations

IAST calculations were performed using the pyIAST Python package to predict mixed-gas adsorption isotherms from pure gas adsorption isotherms.[57] It was assumed that the adsorbates in the mixture were ideal and the adsorption equilibrium between adsorbed and gaseous phases follows the standard state specified by surface potential Φ_i given by the Gibbs adsorption equilibrium (eqn (S2)†).

Molecular simulation

Grand canonical Monte Carlo (GCMC) simulations were performed using the MS©2017 Dassault System 5.0 package [Accelrys Software Inc., San Diego, CA]. IRHs **6** and **7** were considered to be rigid frameworks. The QEq method and QEq_neutral1.0 parameters were used to determine partial charges for atoms in IRHs **6** and **7**. The CO_2 partial charges for atoms were $q(C) = +0.70e$ and $q(O) -0.35e$ ($e = 1.6022 \times 10^{-19}$ C). The interaction energy between the framework and CO_2 was computed using the Coulomb and Lennard-Jones 6-12 (LJ) potentials. A cut-off radius of 15.2 Å was chosen for the LJ potential and Ewald & Group summation method was used to calculate electrostatic interactions between the framework and CO_2 molecules. A value of 1×10^6 was used for all loading,

equilibration and production steps. All simulations were carried out at 298 K.

Author contributions

ME and AD conceived the work. ME and MM carried out all syntheses. ND repeated to verify the synthesis procedure. ME carried out the solvent exchange and the activation of all materials, and performed all characterization techniques (IR, TGA, SEM). TM performed single-crystal X-ray diffraction for all samples. ME performed powder X-ray diffraction for all samples. ME and NF collected gas sorption data. ME carried out all adsorption studies, IAST and GCMC simulation studies. ME and AA carried out the comparison of the adsorption results with those of the reported materials. ME wrote the manuscript. All authors reviewed and edited the manuscript. AD supervised the entire project. All authors have read and agreed to the published version of the manuscript.

Conflicts of interest

The authors declare no competing financial interest.

Acknowledgements

References

1 T. R. Anderson, E. Hawkins and P. D. Jones, CO_2, the greenhouse effect and global warming: From the pioneering work of Arrhenius and Callendar to today's Earth system models, *Endeavour*, 2016, **40**(3), 178–187, DOI: **10.1016/j.endeavour.2016.07.002**.

2 D. J. Couling, U. Das and W. H. Green, Analysis of hydroxide sorbents for CO_2 capture from warm syngas, *Ind. Eng. Chem. Res.*, 2012, **51**(41), 13473–13481, DOI: **10.1021/ie300189a**.

3 J. D. McDonald, D. Kracko, M. Doyle-Eisele, C. E. Garner, C. Wegerski, A. Senft, E. Knipping, S. Shaw and A. Rohr, Carbon capture and sequestration: An exploratory inhalation toxicity assessment of amine-trapping solvents and their degradation products, *Environ. Sci. Technol.*, 2014, **48**(18), 10821–10828, DOI: **10.1021/es5009505**.

4 A. M. Saeed, P. M. Rewatkar, H. Majedi Far, T. Taghvaee, S. Donthula, C. Mandal, C. Sotiriou-Leventis and N. Leventis, Selective CO_2 sequestration with monolithic

This journal is © the Partner Organisations 2023

Inorg. Chem. Front., 2023, **10**, 1037–1048 | **1045**

bimodal micro/macroporous carbon aerogels derived from stepwise pyrolytic decomposition of polyamide–polyimide–polyurea random copolymers, *ACS Appl. Mater. Interfaces*, 2017, **9**(15), 13520–13536, DOI: **10.1021/acsami.7b01910**.

5 J. Zhao, K. Xie, R. Singh, G. Xiao, Q. Gu, Q. Zhao, G. Li, P. Xiao and P. A. Webley, Li+/ZSM-25 zeolite as a CO_2 capture adsorbent with high selectivity and improved adsorption kinetics, showing CO_2-Induced framework expansion, *J. Phys. Chem. C*, 2018, **122**(33), 18933–18941, DOI: **10.1021/acs.jpcc.8b04152**.

6 S. M. W. Wilson and F. H. Tezel, Direct dry air capture of CO_2 using VTSA with faujasite zeolites, *Ind. Eng. Chem. Res.*, 2020, **59**(18), 8783–8794, DOI: **10.1021/acs.iecr.9b04803**.

7 Y. Wang and R. T. Yang, Chemical liquid deposition modified 4A zeolite as a size-selective adsorbent for methane upgrading, CO_2 capture and air separation, *ACS Sustainable Chem. Eng.*, 2019, **7**(3), 3301–3308, DOI: **10.1021/acssuschemeng.8b05339**.

8 Y. Zhou, B. Liu, X. Sun, J. Li, G. Li, Q. Huo and Y. Liu, Self-assembly of homochiral porous supramolecular organic frameworks with significant CO_2 capture and CO_2/N_2 selectivity, *Cryst. Growth Des.*, 2017, **17**(12), 6653–6659, DOI: **10.1021/acs.cgd.7b01282**.

9 X. Cao, Z. Wang, Z. Qiao, S. Zhao and J. Wang, Penetrated COF channels: Amino environment and suitable size for CO_2 preferential adsorption and transport in mixed matrix membranes, *ACS Appl. Mater. Interfaces*, 2019, **11**(5), 5306–5315, DOI: **10.1021/acsami.8b16877**.

10 A. Zulys, F. Yulia, N. Muhadzib and N. Nasruddin, Biological metal–organic frameworks (Bio-MOFs) for CO_2 capture, *Ind. Eng. Chem. Res.*, 2020, **60**(1), 37–51, DOI: **10.1021/acs.iecr.0c04522**, acs.iecr.0c04522.

11 C. Chen, X. Feng, Q. Zhu, R. Dong, R. Yang, Y. Cheng and C. He, Microwave-assisted rapid synthesis of well-shaped MOF-74 (Ni) for CO_2 efficient capture, *Inorg. Chem.*, 2019, **58**(4), 2717–2728, DOI: **10.1021/acs.inorgchem.8b03271**.

12 H. Furukawa, K. E. Cordova, M. O'Keeffe and O. M. Yaghi, The chemistry and applications of metal-organic frameworks, *Science*, 2013, 1230444, DOI: **10.1126/science.1230444**, American Association for the Advancement of Science August 30.

13 A. E. Baumann, D. A. Burns, B. Liu and V. S. Thoi, Metal–organic framework functionalization and design strategies for advanced electrochemical energy storage devices, *Commun. Chem.*, 2019, **2**(1), 1–14, DOI: **10.1038/s42004-019-0184-6**.

14 M. Kotzabasaki and G. E. Froudakis, Review of computer simulations on anti-cancer drug delivery in MOFs, *Inorg. Chem. Front.*, 2018, 1255–1272, DOI: **10.1039/c7qi00645d**, Royal Society of Chemistry June 1.

15 T. W. Duan and B. Yan, Lanthanide Ions (Eu^{3+}, Tb^{3+}, Sm^{3+}, Dy^{3+}) activated ZnO embedded zinc 2,5-pyridinedicarboxylic metal–organic frameworks for luminescence application, *J. Mater. Chem. C*, 2015, **3**(12), 2823–2830, DOI: **10.1039/c4tc02893g**.

16 Ş. Tokalıoğlu, E. Yavuz, S. Demir and Ş. Patat, Zirconium-based highly porous metal–organic framework (MOF-545) as an efficient adsorbent for vortex assisted-solid phase extraction of lead from cereal, beverage and water samples, *Food Chem.*, 2017, **237**, 707–715, DOI: **10.1016/j.foodchem.2017.06.005**.

17 M. Ding, R. W. Flaig, H. L. Jiang and O. M. Yaghi, Carbon capture and conversion using metal–organic frameworks and MOF-based materials, *Chem. Soc. Rev.*, 2019, 2783–2828, DOI: **10.1039/c8cs00829a**, Royal Society of Chemistry May 21.

18 M. T. Kapelewski, T. Runčevski, J. D. Tarver, H. Z. H. Jiang, K. E. Hurst, P. A. Parilla, A. Ayala, T. Gennett, S. A. Fitzgerald, C. M. Brown and J. R. Long, Record high hydrogen storage capacity in the metal–organic framework Ni_2(m-Dobdc) at near-ambient temperatures, *Chem. Mater.*, 2018, **30**(22), 8179–8189, DOI: **10.1021/acs.chemmater.8b03276**.

19 Y. An, Y. Liu, H. Bian, Z. Wang, P. Wang, Z. Zheng, Y. Dai, M.-H. Whangbo and B. Huang, Improving the photo-catalytic hydrogen evolution of UiO-67 by incorporating Ce^{4+}-coordinated bipyridinedicarboxylate ligands, *Sci. Bull.*, 2019, **64**(20), 1502–1509, DOI: **10.1016/j.scib.2019.07.030**.

20 Y. Xiao, W. Wei, M. Zhang, S. Jiao, Y. Shi and S. Ding, Facile surface properties engineering of high-quality graphene: Toward advanced Ni-MOF heterostructures for high-performance supercapacitor electrode, *ACS Appl. Energy Mater.*, 2019, **2**(3), 2169–2177, DOI: **10.1021/acsaem.8b02201**.

21 M. Yu, Y. Xie, X. Wang, Y. Li and G. Li, Highly water-stable dye@Ln-MOFs for sensitive and selective detection toward antibiotics in water, *ACS Appl. Mater. Interfaces*, 2019, **11**(23), 21201–21210, DOI: **10.1021/acsami.9b05815**.

22 N. Dissem, M. Essalhi, N. Ferhi, A. Abidi, T. Maris and A. Duong, Flexible and porous 2D layered structures based on mixed-linker metal–organic frameworks for gas sorption studies, *Dalton Trans.*, 2021, **50**, 8727–8735, DOI: **10.1039/d1dt00426c**.

23 P. M. Bhatt, Y. Belmabkhout, A. Cadiau, K. Adil, O. Shekhah, A. Shkurenko, L. J. Barbour and M. Eddaoudi, A fine-tuned fluorinated MOF addresses the needs for trace CO_2 removal and air capture using physisorption, *J. Am. Chem. Soc.*, 2016, **138**(29), 9301–9307, DOI: **10.1021/jacs.6b05345**.

24 Y. Li, X. Zhang, J. Lan, P. Xu and J. Sun, Porous Zn (Bmic) (AT) MOF with abundant amino groups and open metal sites for efficient capture and transformation of CO_2, *Inorg. Chem.*, 2019, **58**(20), 13917–13926, DOI: **10.1021/acs.inorgchem.9b01762**.

25 H. Jiang, D. Alezi and M. Eddaoudi, A reticular chemistry guide for the design of periodic solids, *Nat. Rev. Mater.*, 2021, **6**(6), 466–487, DOI: **10.1038/s41578-021-00287-y**.

26 H. Daglar and S. Keskin, Computational screening of metal–organic frameworks for membrane-based $CO_2/N_2/$ H_2O separations: Best materials for flue gas separation, *J. Phys. Chem. C*, 2018, **122**(30), 17347–17357, DOI: **10.1021/acs.jpcc.8b05416**.

1046 | *Inorg. Chem. Front.*, 2023, **10**, 1037–1048

This journal is © the Partner Organisations 2023

27 W. Fan, S. Yuan, W. Wang, L. Feng, X. Liu, X. Zhang, X. Wang, Z. Kang, F. Dai, D. Yuan, D. Sun and H.-C. Zhou, Optimizing multivariate metal–organic frameworks for efficient C_2H_2/CO_2 separation, *J. Am. Chem. Soc.*, 2020, **142**(19), 8728–8737, DOI: **10.1021/jacs.0c00805**.

28 E. D. Bloch, M. R. Hudson, J. A. Mason, S. Chavan, V. Crocellà, J. D. Howe, K. Lee, A. L. Dzubak, W. L. Queen, J. M. Zadrozny, S. J. Geier, L. C. Lin, L. Gagliardi, B. Smit, J. B. Neaton, S. Bordiga, C. M. Brown and J. R. Long, Reversible CO binding enables tunable CO/H_2 and CO/N_2 separations in metal–organic frameworks with exposed divalent metal cations, *J. Am. Chem. Soc.*, 2014, **136**(30), 10752–10761, DOI: **10.1021/ja505318p**.

29 D. J. Xiao, M. I. Gonzalez, L. E. Darago, K. D. Vogiatzis, E. Haldoupis, L. Gagliardi and J. R. Long, Selective, tunable O_2 binding in cobalt(II)-triazolate/pyrazolate metal–organic frameworks, *J. Am. Chem. Soc.*, 2016, **138**(22), 7161–7170, DOI: **10.1021/jacs.6b03680**.

30 Z. R. Herm, J. A. Swisher, B. Smit, R. Krishna and J. R. Long, Metal–organic frameworks as adsorbents for hydrogen purification and precombustion carbon dioxide capture, *J. Am. Chem. Soc.*, 2011, **133**(15), 5664–5667, DOI: **10.1021/ja111411q**.

31 Z. Bao, L. Yu, Q. Ren, X. Lu and S. Deng, Adsorption of CO_2 and CH_4 on a magnesium-based metal organic framework, *J. Colloid Interface Sci.*, 2011, **353**(2), 549–556, DOI: **10.1016/j.jcis.2010.09.065**.

32 M. Mohan, T. Maris and A. Duong, Building coordination polymers using dipyridone ligands, *CrystEngComm*, 2020, **22**(3), 441–447, DOI: **10.1039/c9ce01725a**.

33 M. Mohan, M. Essalhi, D. Durette, L. K. Rana, F. K. Ayevide, T. Maris and A. Duong, A rational design of microporous nitrogen-rich lanthanide metal–organic frameworks for CO_2/CH_4 separation, *ACS Appl. Mater. Interfaces*, 2020, **12**(45), 50619–50627, DOI: **10.1021/acsami.0c15395**.

34 M. Essalhi, M. Mohan, G. Marineau-Plante, A. Schlachter, T. Maris, P. D. Harvey and A. Duong, S-Heptazine, N-ligand based luminescent coordination materials: Synthesis, structural and luminescent studies of lanthanide–cyamelurate networks, *Dalton Trans.*, 2022, **51**(39), 15005–15016, DOI: **10.1039/D2DT01924H**.

35 A. L. Spek, Single-crystal structure validation with the program PLATON, *J. Appl. Crystallogr.*, 2003, **36**, 7–13.

36 D. Gnanasekaran and B. S. R. Reddy, Cost effective poly (urethane-imide)-POSS membranes for environmental and energy-related processes, *Clean Technol. Environ. Policy*, 2012, **15**(2), 383–389, DOI: **10.1007/S10098-012-0500-7**.

37 S. Mohammed, A. K. Sunkara, C. E. Walike and G. Gadikota, The role of surface hydrophobicity on the structure and dynamics of CO_2 and CH_4 confined in silica nanopores, *Front. Climate*, 2021, **3**, 80, DOI: **10.3389/FCLIM.2021.713708/BIBTEX**.

38 D. Frenkel and B. Smit, *Understanding Molecular Simulation: From Algorithms to Applications*, Elsevier, 2001, vol. 1, p. 638.

39 T. Pham, K. A. Forrest, A. Hogan, B. Tudor, K. McLaughlin, J. L. Belof, J. Eckert and B. Space, Understanding hydrogen sorption in In-Soc-MOF: A charged metal–organic framework with open-metal sites, narrow channels, and counterions, *Cryst. Growth Des.*, 2015, **15**(3), 1460–1471, DOI: **10.1021/CG5018104/SUPPL_FILE/CG5018104_SI_001.PDF**.

40 T. Pham, K. A. Forrest, D. M. Franz and B. Space, Experimental and theoretical investigations of the gas adsorption sites in Rht-metal–organic frameworks, *CrystEngComm*, 2017, **19**(32), 4646–4665, DOI: **10.1039/C7CE01032J**.

41 A. L. Myers and J. M. Prausnitz, Thermodynamics of mixed-gas adsorption, *AIChE J.*, 1965, **11**(1), 121–127, DOI: **10.1002/aic.690110125**.

42 C. M. Simon, B. Smit and M. Haranczyk, PyIAST: Ideal adsorbed solution theory (IAST) Python package, *Comput. Phys. Commun.*, 2016, **200**, 364–380, DOI: **10.1016/j.cpc.2015.11.016**.

43 J. Wang, Y. Wei and Z. Ma, Modified dual-site Langmuir adsorption equilibrium models from a GCMC molecular simulation, *Appl. Sci.*, 2020, **10**(4), 1311, DOI: **10.3390/APP10041311**.

44 Y. Chen, H. Wu, Z. Liu, X. Sun, Q. Xia and Z. Li, Liquid-assisted mechanochemical synthesis of copper based MOF-505 for the separation of CO_2 over CH_4 or N_2, *Ind. Eng. Chem. Res.*, 2018, **57**(2), 703–709, DOI: **10.1021/acs.iecr.7b03712**.

45 G. Wang, K. Leus, H. S. Jena, C. Krishnaraj, S. Zhao, H. Depauw, N. Tahir, Y. Y. Liu and P. van der Voort, A fluorine-containing hydrophobic covalent triazine framework with excellent selective CO_2 capture performance, *J. Mater. Chem. A*, 2018, **6**(15), 6370–6375, DOI: **10.1039/c7ta08913a**.

46 G. Avci, S. Velioglu and S. Keskin, High-throughput screening of MOF adsorbents and membranes for H_2 purification and CO_2 capture, *ACS Appl. Mater. Interfaces*, 2018, **10**(39), 33693–33706, DOI: **10.1021/acsami.8b12746**.

47 S. Xiang, Y. He, Z. Zhang, H. Wu, W. Zhou, R. Krishna and B. Chen, Microporous metal–organic framework with potential for carbon dioxide capture at ambient conditions, *Nat. Commun.*, 2012, **3**(1), 1–9, DOI: **10.1038/ncomms1956**.

48 B. Ashourirad, A. K. Sekizkardes, S. Altarawneh and H. M. El-Kaderi, Exceptional gas adsorption properties by nitrogen-doped porous carbons derived from benzimidazole-linked polymers, *Chem. Mater.*, 2015, **27**(4), 1349–1358, DOI: **10.1021/cm504435m**.

49 H. M. Wen, C. Liao, L. Li, A. Alsalme, Z. Alothman, R. Krishna, H. Wu, W. Zhou, J. Hu and B. Chen, A metal–organic framework with suitable pore size and dual functionalities for highly efficient post-combustion CO_2 capture, *J. Mater. Chem. A*, 2019, **7**(7), 3128–3134, DOI: **10.1039/c8ta11596f**.

50 J. McEwen, J. D. Hayman and A. Ozgur Yazaydin, A comparative study of CO_2, CH_4 and N_2 adsorption in ZIF-8, Zeolite-13X and BPL activated carbon, *Chem. Phys.*, 2013, **412**, 72–76, DOI: **10.1016/j.chemphys.2012.12.012**.

This journal is © the Partner Organisations 2023

Inorg. Chem. Front., 2023, **10**, 1037–1048 | **1047**

51 G. M. Sheldrick, SHELXT – Integrated space-group and crystal-structure determination, *Acta Crystallogr., Sect. A: Found. Adv.*, 2015, **71**(1), 3–8, DOI: **10.1107/S2053273314026370**.

52 G. M. Sheldrick, Crystal structure refinement with SHELXL, *Acta Crystallogr., Sect. C: Struct. Chem.*, 2015, **71**(1), 3–8, DOI: **10.1107/S2053229614024218**.

53 C. F. Macrae, P. R. Edgington, P. McCabe, E. Pidcock, G. P. Shields, R. Taylor, M. Towler and J. van de Streek, Mercury: Visualization and analysis of crystal structures, *J. Appl. Crystallogr*, 2006, **39**, 453–457, DOI: **10.1107/S002188980600731X**, International Union of Crystallography June 10, 2006.

54 E. Horvath-Bordon, E. Kroke, I. Svoboda, H. Fueß, R. Riedel, S. Neeraj and A. K. Cheetham, Alkalicyamelurates, $M_3[C_6N_7O_3] \cdot xH_2O$, M = Li, Na, K, Rb, Cs: UV-luminescent and thermally very stable ionic Tris-triazine derivatives, *Dalton Trans.*, 2004, (No. 22), 3900–3908, DOI: **10.1039/b412517g**.

55 F. A. Kloutse, A. Hourri, S. Natarajan, P. Benard and R. Chahine, Hydrogen separation by adsorption: Experiments and modelling of H_2-N_2-CO_2 and H_2-CH_4-CO_2 mixtures adsorption on CuBTC and MOF-5, *Microporous Mesoporous Mater.*, 2018, **271**, 175–185, DOI: **10.1016/j.micromeso.2018.05.042**.

56 F. A. Kloutse, A. Hourri, S. Natarajan, P. Benard and R. Chahine, Experimental benchmark data of CH_4, CO_2 and N_2 binary and ternary mixtures adsorption on MOF-5, *Sep. Purif. Technol.*, 2018, **197**, 228–236, DOI: **10.1016/j.seppur.2018.01.013**.

57 C. M. Simon, B. Smit and M. Haranczyk, PyIAST: Ideal adsorbed solution theory (IAST) Python package, *Comput. Phys. Commun.*, 2016, **200**, 364–380, DOI: **10.1016/J.CPC.2015.11.016**.